2013 IEEE International Conference on Robotics and Automation (ICRA)
Karlsruhe, Germany, May 6-10, 2013

Identification of Flight Aerodynamics for Flapping-Wing Microrobots

Pakpong Chirarattananon and Robert J Wood

Abstract— **Experimentally collected flight dynamics data of flapping-wing microrobots reveals several characteristics that cannot be captured by the information gathered from static experiments. For an insect-sized flapping-wing micro air vehicle with air dampers, we show that a physics-based quasi-steady aerodynamic model is able to predict the flight dynamics with reasonable accuracy. The proposed model is optimized for the vehicle of interest through the use of learning algorithms. The identified model demonstrates the potential for future use in control applications.**

I. Introduction

In recent years, a new class of biologically-inspired flapping-wing micro aerial vehicles has emerged [1], [2], [3], including the Harvard RoboBee that has demonstrated controlled vertical flight [4]. Advances in mesoscale manufacturing technology has allowed researchers to create robotic insects capable of producing sufficient lift force for flight and control experiments [5], [6].

The design of the RoboBee in [4] is severely underactuated and unable to produce roll and yaw torques for control purposes. More recent prototypes have incorporated additional actuators and are capable of producing all rotational torques [7], [8]. However, these designs still have varying degrees of underactuation and are all inherently unstable. In [6], it is demonstrated that the addition of air dampers to a severely underactuated robotic bee provides adequate passive stability for vertical liftoff and short controlled flights. The presence of passive dampers radically alters the flight dynamics of the robot. A simple linear two-dimensional model was proposed as a design guideline for achieving upright stability. It is, however, not sufficiently accurate to explain the dynamics of the vehicle captured from the motion tracking system used in the experiment.

Understanding the role of the dampers is, therefore, crucial to progress in the control of the vehicles. Incorporation of dampers could aid the control effort by dramatically slowing down the dynamics and countering inherent force and torque biases from fabrication imperfections. This prompts the need to study the aerodynamic effects of the dampers in flapping-wing flight.

This work was partially supported by the National Science Foundation (award number CCF-0926148), and the Wyss Institute for Biologically Inspired Engineering. Any opinions, findings, and conclusions or recommendations expressed in this material are those of the authors and do not necessarily reflect the views of the National Science Foundation.

The authors are with the School of Engineering and Applied Sciences, Harvard University, Cambridge, MA 02138, USA, and the Wyss institute for Biologically Inspired Engineering, Harvard University, Boston, MA, 02115, USA (email: chirarat@fas.harvard.edu; rjwood@eecs.harvard.edu).

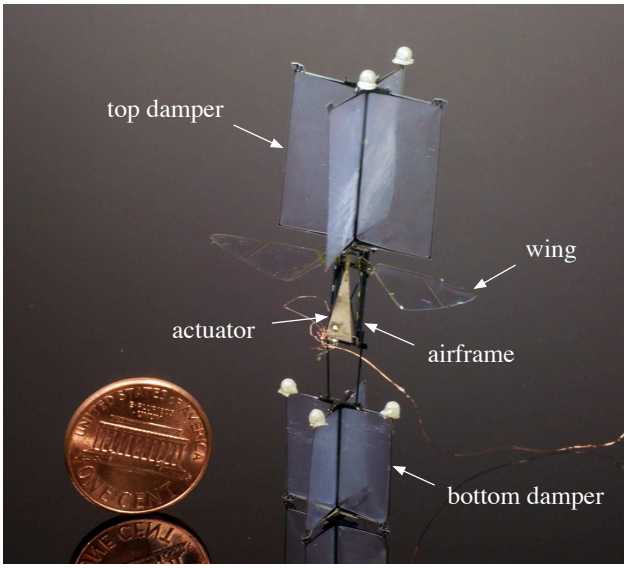

Fig. 1. A photograph of a robotic bee with air dampers. The total vehicle weighs 121 mg including five retroreflective markers for the visual tracking system.

In this work, we seek to characterize the flight dynamics of a robotic bee with dampers attached. The robot employed for the experiment is illustrated in Fig. 1, almost identical to those in [4], [6], and similar to recently developed counterparts scale-wise [7], [8]. To achieve this, a physics-based aerodynamic model is proposed. Learning techniques are then utilized to identify unknown parameters such that the discrepancy between the model predictions and the body state extracted from recorded trajectories is minimized. Since the model accounts for the effects from both translational and rotational dynamics of the vehicle, such information cannot be acquired in a quasi-static wind tunnel experiment.

Due to the inherent instabilities and fast dynamics of these vehicles, to be useful, this model must encompass all operating conditions. In other words, it is not linearized about hovering or forward flight, thus leading to a highly nonlinear behavior. This approach is, therefore, distinct from literature on aircraft system identification, where the models are typically linearized around cruising conditions [9], [10]. As a result, in this work, time domain identification techniques are employed [11], [12], [13], instead of frequency domain methods [9], [10], [14].

The physics-based approach taken here is unlikely to capture the dynamics of the vehicle as accurately as a

model composed of best-fitted basis functions as presented in [10], [11], [13], nevertheless, it offers more insights into the interactions between aerodynamic forces and individual components of the vehicle. As a consequence, the learned model could serve as a guideline to iterate the design of the vehicle for better performance.

The rest of the paper is organized as follows. Section II briefly outlines the convention used to describe the flight dynamics. The proposed aerodynamic model is detailed in Section III. Section IV covers the identification method and its implementation. This includes the results and the comparison between the measurements and the predictions made by the proposed model. Finally, further considerations and future work are discussed in Section V.

II. Flight Dynamics

The robotic insect is regarded as a rigid body in three-dimensional space. The state vector $\mathbf{X}$ comprises twelve parameters; velocity in the body frame ($\dot{x}$,$\dot{y}$,$\dot{z}$), Euler angles representing the rotation between the body frame and the inertial frame (α, β, γ), angular velocity $(\omega_x, \omega_y, \omega_z)$, and position in the inertial frame (X, Y, Z) as illustrated in Fig. 2.

$$\mathbf{X} = \begin{bmatrix} \dot{x} & \dot{y} & \dot{z} & \alpha & \beta & \gamma & \omega_x & \omega_y & \omega_z & X & Y & Z \end{bmatrix}^T \tag{1}$$

The orientation between the body frame and the inertial frame is related by a rotation matrix, written as sequential rotations by Euler angles (α, β, γ) about their respective axes [15].

$$\begin{bmatrix} X \\ Y \\ Z \end{bmatrix} = R_x(\alpha)R_y(\beta)R_z(\gamma) \begin{bmatrix} x \\ y \\ z \end{bmatrix} \tag{2}$$

The dynamics of the state $\mathbf{X}$ are nonlinear and governed by equation (3), which can be separated into four terms in equations (4)-(7).

$$\frac{d}{dt}\mathbf{X} = f(\mathbf{X}) \tag{3}$$

Accelerations of the body frame are caused by the total force acting on the body of mass m and the coriolis force as shown in equation (4). Here the total force ΣF is a summation of aerodynamic damping F^d, thrust generated from the robot F^t and gravitational force F^g along each body axis.

$$\frac{d}{dt}\begin{bmatrix} \dot{x} \\ \dot{y} \\ \dot{z} \end{bmatrix} = \frac{1}{m}\begin{bmatrix} \Sigma F_x - m(\omega_y\dot{z} - \omega_z\dot{y}) \\ \Sigma F_y - m(\omega_z\dot{x} - \omega_x\dot{z}) \\ \Sigma F_z - m(\omega_x\dot{y} - \omega_y\dot{x}) \end{bmatrix} \tag{4}$$

The dynamics of three Euler angles are dependent on the angular velocity as follows:

$$\frac{d}{dt}\begin{bmatrix} \alpha \\ \beta \\ \gamma \end{bmatrix} = \begin{bmatrix} \frac{\cos\gamma}{\cos\beta} & -\frac{\sin\gamma}{\cos\beta} & 0 \\ \sin\gamma & \cos\gamma & 0 \\ -\frac{\sin\beta\cos\gamma}{\cos\beta} & \frac{\sin\beta\sin\gamma}{\cos\beta} & 1 \end{bmatrix}\begin{bmatrix} \omega_x \\ \omega_y \\ \omega_z \end{bmatrix}, \tag{5}$$

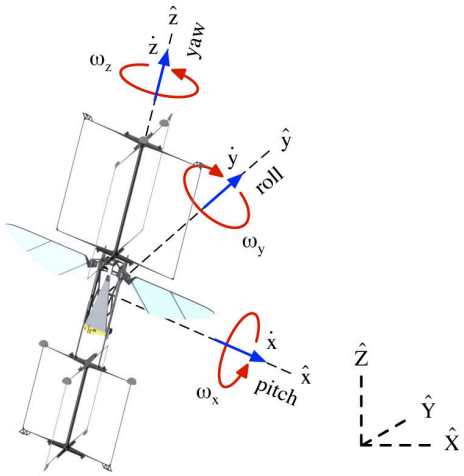

Fig. 2. Schematic illustration of the microrobotic bee employed in this work. The body frame ($\hat{x}$, $\hat{y}$, and $\hat{z}$) are related to the fixed coordinates ($\hat{X}$, $\hat{Y}$, and $\hat{Z}$) is three Euler angles α, β, and γ. The vehicle is moving at the velocity defined by $\dot{x}$, $\dot{y}$, and $\dot{z}$ with respect to the body frame and its pitch, roll, and yaw rate are given by ω_x, ω_y, and ω_z.

while the angular acceleration is given by Euler equations, as a function of the total torques along the body axes:

$$\frac{d}{dt}\begin{bmatrix} \omega_x \\ \omega_y \\ \omega_z \end{bmatrix} = \begin{bmatrix} [\Sigma\tau_x - (I_{zz} - I_{yy})\omega_y\omega_z]\, I_{xx}^{-1} \\ [\Sigma\tau_y - (I_{xx} - I_{zz})\omega_x\omega_z]\, I_{yy}^{-1} \\ [\Sigma\tau_z - (I_{yy} - I_{xx})\omega_x\omega_y]\, I_{zz}^{-1} \end{bmatrix}. \tag{6}$$

Again, the total torque $\Sigma\tau$ is from aerodynamic damping τ^d, and thrust τ^t. I_{xx}, I_{yy}, and I_{zz} are the moments of inertia along the three principal axes. It is assumed that the cross terms are negligibly small owing to the symmetry of the vehicle.

Lastly the velocity in the world frame is given by the time derivative of equation (2).

$$\frac{d}{dt}\begin{bmatrix} X \\ Y \\ Z \end{bmatrix} = R_x(\alpha)R_y(\beta)R_z(\gamma)\begin{bmatrix} \dot{x} \\ \dot{y} \\ \dot{z} \end{bmatrix} \tag{7}$$

Hence, given the current state vector and all force and torque information, it is possible to evaluate future states via equations (4)-(7).

III. Aerodynamic Model

A linearized model of the aerodynamics of the dampers was proposed in [6], based on previous work in [16]. In both cases, however, the analyses were greatly simplified and limited to a two-dimensional approximation. In this section, we propose a physics-based quasi-steady aerodynamic model to account for the aerodynamic damping caused by the flapping wings and dampers as a result of translation and rotation in three-dimensional space.

Based on the geometry of the dampers and the wings, and the low Reynolds number (≈1000), it is appropriate to employ *flat plate theory* as an analysis tool. In [11], [17], it was shown that this method is capable of accurately predicting the aerodynamics of UAV perching under unsteady flight regimes.

Flat plate theory implies that the total drag force is perpendicular to a flat plate, and dependent on the flow velocity perpendicular to the surface. That is

$$F = -\rho S v_\perp |v_\perp|, \tag{8}$$

where ρ is the ambient air density, S is the area of the plate, and $v_\perp$ is the component of the flow velocity perpendicular to the plate.

To account for variation of flow velocity across an airfoil, the *blade element method* allows us to break the airfoil into small parts and determine the forces on each small element. The forces are then integrated over the entire airfoil to obtain the total forces and torques. In [18], [19] the predictions from the blade element approach have shown strong agreement with experimental measurements for rotational wing dynamics. In this work, using equation (8) and the blade element method, the resultant force acting upon an airfoil is taken to be

$$F = -\rho C \int v_\perp(\cdot) |v_\perp(\cdot)| \, dS, \tag{9}$$

where $v_\perp(\cdot)$ represents a perpendicular local flow velocity at the areal element dS. Note the incorporation of C as an additional dimensionless parameter to account for unconsidered aerodynamic effects, such as unsteady flow features, and simplifications of the model. In other words, C would be unity if this theoretical model is perfect.

A. Damper contribution

The force and torque contribution from the dampers can be evaluated according to equation (9). To demonstrate this, consider the top damper on the plane normal to the $\hat{y}$-axis as presented in Fig. 3a. The corresponding contribution to the damping force along $\hat{y}$ is given by

$${}^t F_y^d = -\rho C_t \int v_\perp(P) |v_\perp(P)| \, dS, \tag{10}$$

where P represents a point on the damper at the distance r and h away from the center of mass along $\hat{x}$ and $\hat{z}$ axes as depicted in Fig. 3a, C_t is a force coefficient for the top damper, and ${}^t F_y^d$ is the aerodynamic force along $\hat{y}$ contributed by the top damper.

Since the local flow velocity at point P can be written as a function of the position and a few state parameters, equation (10) can be re-written as

$$\begin{aligned} {}^t F_y^d = & -\rho C_t \int_{h=d_t-l_t/2}^{d_t+l_t/2} \int_{r=-l_t/2}^{l_t/2} (\dot{y} - \omega_x h + \omega_z r) \\ & \times |\dot{y} - \omega_x h + \omega_z r| \, dh dr, \end{aligned} \tag{11}$$

where d_t is the distance from the center of mass of the robotic insect to the center of the top damper, and l_t is the width of the square top damper.

It is straightforward to obtain an analytic solution to equation (11). Though, for the sake of simplicity and tractability, here we opt to replace the integration with a finite sum by dividing the damper into two pieces, separated by the $\hat{z}$-axis.

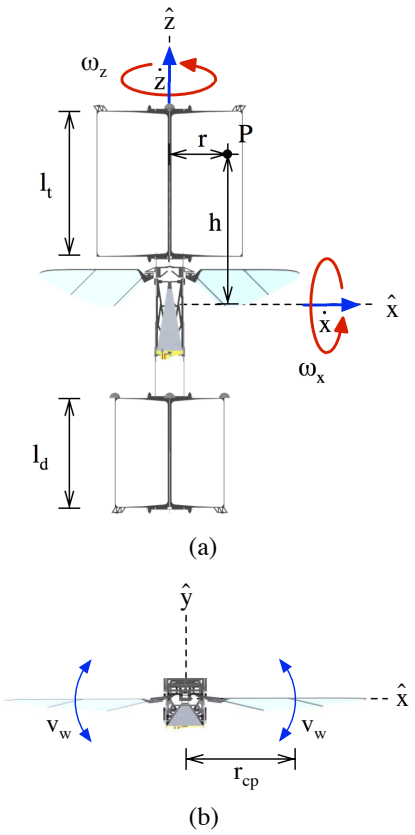

Fig. 3. Diagrams illustrating the geometry of the robotic bee with dampers. (a) At point P on the damper, the perpendicular air speed can be written as a function of $\dot{y}$, $\omega_x h$ and $\omega_z r$. Total aerodynamic force is a summation from all points on the damper. (b) The contribution from flapping wings is considered at mid-stroke, with nominal flapping velocity v_w.

On the assumption that the center of pressure of each piece is approximately at its geometric center, the force contribution from the top damper along the $\hat{y}$-axis is therefore

$$\begin{aligned} {}^t F_y^d = & -\frac{1}{2}\rho C_t l_t^2 \\ & \times \left[\left| \dot{y} - \omega_x d_t + \omega_z \frac{l_t}{4} \right| \left(\dot{y} - \omega_x d_t + \omega_z \frac{l_t}{4} \right) \right. \\ & \left. + \left| \dot{y} - \omega_x d_t - \omega_z \frac{l_t}{4} \right| \left(\dot{y} - \omega_x d_t - \omega_z \frac{l_t}{4} \right) \right]. \end{aligned} \tag{12}$$

The error introduced by this approximation can be partially absorbed into the force coefficient C_t.

The above procedure can be applied to calculate the torque caused by the damper:

$$\begin{aligned} {}^{t,y}\tau_z^d = & -\frac{1}{8}\rho C_t l_t^3 \\ & \times \left[\left| \dot{y} - \omega_x d_t + \omega_z \frac{l_t}{4} \right| \left(\dot{y} - \omega_x d_t + \omega_z \frac{l_t}{4} \right) \right. \\ & \left. - \left| \dot{y} - \omega_x d_t - \omega_z \frac{l_t}{4} \right| \left(\dot{y} - \omega_x d_t - \omega_z \frac{l_t}{4} \right) \right]. \end{aligned} \tag{13}$$

Note that the superscript t, y indicates that this torque is a result of drag on the piece perpendicular to the $\hat{y}$-axis of the top damper, while the subscript z denotes that the torque is about the $\hat{z}$-axis.

The same calculation can also be carried out for other directions. In total, the force and torque contribution from the top damper can be summarized as functions of required state parameters as follows:

$$\begin{bmatrix} {}^{t}F_x^d \\ {}^{t}F_y^d \\ {}^{t}F_z^d \end{bmatrix} = \begin{bmatrix} {}^{t}F_x^d\left(C_t, \dot{x}, \omega_y, \omega_z\right) \\ {}^{t}F_y^d\left(C_t, \dot{y}, \omega_x, \omega_z\right) \\ 0 \end{bmatrix} \tag{14}$$

$$\begin{bmatrix} {}^{t}\tau_x^d \\ {}^{t}\tau_y^d \\ {}^{t}\tau_z^d \end{bmatrix} = \begin{bmatrix} {}^{t}\tau_x^d\left(C_t, \dot{y}, \omega_x, \omega_z\right) \\ {}^{t}\tau_y^d\left(C_t, \dot{x}, \omega_y, \omega_z\right) \\ {}^{t,x}\tau_z^d\left(C_t, \dot{x}, \omega_y, \omega_z\right) \\ \quad + {}^{t,y}\tau_z^d\left(C_t, \dot{y}, \omega_x, \omega_z\right) \end{bmatrix} \tag{15}$$

The contribution from the bottom damper can be determined in a similar fashion with C_t and d_t replaced by C_b and d_b, and the distance from the center of mass to the center of the bottom damper, d_b, is a negative value. It can be seen that, assuming flat plate theory, the dampers do not play a part in damping along the $\hat{z}$-axis.

B. Wing contribution

The interaction between flapping wings and the ambient air poses a complicated aerodynamic problem. The aerodynamic effects of passive rotational dynamics have also been intensively studied [19], [20]. Here, ignoring the passive rotation and relying on a few assumptions, we propose a simplified model to explain the effects of flapping wings under the translational and rotational dynamics of the vehicle.

To begin with, let the nominal linear speed of the flapping wings at mid-stroke at the center of pressure be v_w as shown in Fig. 3b. The distance from the center of pressure of the wing to the center of mass is r_{cp} along the $\hat{z}$-axis and d_w along the $\hat{x}$-axis. v_w is a quantity that depends on the flapping frequency f and flapping amplitude Φ. The true flow velocity acting on each wing is a function of v_w and the current translational and rotational velocity of the robot. In this circumstance, it is assumed that the aerodynamic effects due to flapping can be taken at mid-stroke, where the relative flow velocity is greatest.

We are interested in the stroke-averaged force and torque. The resultant force turns out to be linear with the flow velocity. Effectively, flapping wings can be regarded as a pair of flat plates moving in a plane perpendicular to the $\hat{z}$-axis that result in linear damping. A similar analysis can also be found in [6].

Furthermore, a pair of flapping wings was found, under wind tunnel experiments, to produce comparable drag in both lateral ($\hat{x}$) and forward ($\hat{y}$) directions [6]. Taking this into consideration, with the same approach used in section III-A, the flapping wings contribute to aerodynamic damping as follows:

$$\begin{bmatrix} {}^{w}F_x^d \\ {}^{w}F_y^d \\ {}^{w}F_z^d \end{bmatrix} = -4\rho C_w S_w v_w \begin{bmatrix} \dot{x} + \omega_y d_w \\ \dot{y} - \omega_x d_w \\ 0 \end{bmatrix} \tag{16}$$

$$\begin{bmatrix} {}^{w}\tau_x^d \\ {}^{w}\tau_y^d \\ {}^{w}\tau_z^d \end{bmatrix} = -4\rho C_w S_w v_w \begin{bmatrix} (-\dot{y} + \omega_x d_w) d_w \\ (\dot{x} + \omega_y d_w) d_w \\ 2\omega_z r_{cp}^2 \end{bmatrix} \tag{17}$$

where S_w is the planform area of each wing and C_w is a drag coefficient for the wings.

C. Vertical damping force

Thus far, there has been no contribution from the dampers or flapping wings to the damping force along the $\hat{z}$-axis. Partially, this is because the dampers are assumed to be vertically orientated along the body of the robot. In reality, in addition to the effects from the body of the vehicle, it is expected there would be some skin friction and misalignments or structural bending that would lead to the damping along the $\hat{z}$-axis.

Consider a flat plate lying at some angle with respect to the $\hat{z}$-axis, both vertical velocity $\dot{z}$ and yaw rotation ω_z would contribute to the vertical damping. Depending on the angle and the rotation direction, ω_z may contribute to the damping along or opposite $\dot{z}$. Taking into account the quadratic behavior of the aerodynamic damping, we propose that the vertical damping force can be written as an aggregate of three terms.

$$F_z^d = -c_z \left|\dot{z}\right| \dot{z} - c_{z\omega} \dot{z} \omega_z - c_{z\omega^2} \left|\omega_z\right| \omega_z \tag{18}$$

While c_z is strictly a positive number, c_{zw} and $c_{z\omega^2}$ could be negative due to the reason explained above. Note that they are not dimensionless and their values can be determined empirically.

D. Additional yaw damping

In section III-C, it is argued that yaw rotation ω_z contributes to vertical damping. The converse is also true. That is, vertical movement would also result in a torque about the $\hat{z}$-axis if the dampers are not perfectly vertically aligned with the body of the robot. It is, therefore, reasonable to introduce an extra term in the damping along the $\hat{z}$-axis similar to the second term present in equation (18). This yields the total aerodynamic yaw damping:

$$\tau_z^d = {}^{t}\tau_z^d + {}^{b}\tau_z^d + {}^{w}\tau_z^d - c_{\omega z} \dot{z} \omega_z. \tag{19}$$

Again, the parameter $c_{\omega z}$ is to be found experimentally.

IV. Identification

The primary purpose of this work is to identify parameters for the proposed aerodynamic model that correspond to observed trajectories of the vehicle. First, flight data is gathered in an open-loop configuration. Second, necessary preprocessing is performed prior to fitting the model to the measurement data. Finally, we fit and refine the model in a least-squares sense. Each of these steps are described below.

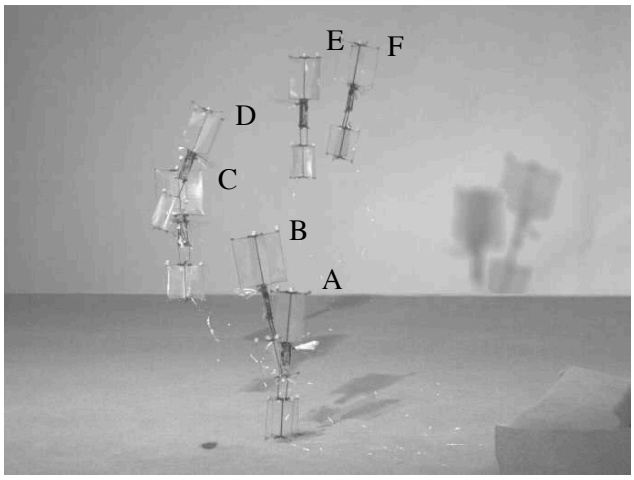

Fig. 4. A composite image from frames of a high speed video of a liftoff flight. The interval between frames is 0.2s. The letters indicate the the order of the frames.

A. Experimental setup

The prototype of a flapping-wing microrobot, shown in Fig. 1, performs 12 uncontrolled flights in this experiment. A composite image illustrating one of the flights is presented in Fig. 4. In each flight, the piezoelectric actuator is driven by a sinusoidal signal at constant amplitude, the peak-to-peak voltage ranges from 250V to 270V across all 12 flights. The reason for the increased drive amplitude is to demonstrate the versatility of the model under different conditions and to compensate for any decrease in lift force due to mechanical fatigue. The flapping frequency is fixed at the system's resonant frequency of 110Hz. The power wires (less than 10mg in weight) are manufactured to be considerably longer than 30cm, enough to cover a reasonable flight volume, and should not affect the flight dynamics (when it is slack).

The test bed is equipped with four *VICON* cameras for visual tracking. The tracking system is operated at 500Hz, covering the volume of $0.3 \times 0.3 \times 0.3$m. The latency of the system ($\approx$10ms) does not affect the experiment performed in open-loop. The motion tracker records the microrobot's position (X, Y, Z) and orientation (α, β, γ) for an offline identification process.

B. Preprocessing

In preprocessing, portions of the flight data where thrust forces and torques are approximately constant are selected. As a result, the data at the beginning of flights prior to takeoff, where forces are ramping up, is discarded. The same applies for the ending to ensure the absence of tension from the wires. This yields 12 sets of data with the average length of 0.274 ± 0.064s, spanning 3.288s or 355 wing beats in total.

Then, the Euler angles, which are recorded in the interval $[0, 2\pi)$, are unwrapped. The data is up-sampled to 1000Hz using a cubic spline to enhance the continuity. These enable us to smooth the trajectories by acausally applying a 3^{rd} order Chebyshev type II low-pass filter to the data sequence. The cutoff frequency of the filter is chosen to be 40Hz in order to filter out the vibrations caused by flapping wings at 110Hz.

The filtered data sets are then numerically differentiated twice to construct a state vector $\mathbf{X}$ and its time derivative according to equations (4)-(7).

C. Least-squares optimization

After the collected data has been preprocessed, we have measurements of $\mathbf{X}$ and its time derivative. Based on the flight dynamics equations in section II and the proposed aerodynamic model in section III, it is also possible to predict $d\mathbf{X}/dt$ from the current state $\mathbf{X}$ as in equation (3). The difference between the measurements and the predictions is a residual error r. The goal is, therefore, to find a set of parameters Θ that minimizes the average residual error S in the least-squares sense.

$$\begin{aligned} r_i &= \frac{d}{dt}\mathbf{X}_i\Big|_{measurement} - \frac{d}{dt}\mathbf{X}_i\Big|_{prediction} \\ \Theta^* &= \underset{\Theta}{\operatorname{argmin}}\ S \\ &= \underset{\Theta}{\operatorname{argmin}}\ \frac{1}{N}\sum_{i=1}^{N} r_i^T W^2 r_i, \end{aligned} \tag{20}$$

where the index i is used to label an element in a sequence. W is a pre-defined diagonal weighting matrix. The summation is for all points in the sequence (1 to N). Note that all 12 flights have been consolidated into one sequence, yielding $N = 3,288$.

The minimization in equation (20) can be carried out in various ways. In this work, since computational speed is not a priority, the method of steepest descent is employed. Moreover, the optimization could be performed relatively efficiently since the availability of analytical expressions for the dynamics allows us to calculate Jacobian matrices directly. Parameters to optimize include force coefficients for aerodynamic effects, moments of inertia, and distances to the center of mass as presented in Table I. Values of other known physical parameters are also listed in the table.

To clarify, one optimization is conducted for all 12 flights. In other words, we seek to find one set of parameters that fits all data. Thrust forces and torques are set to be constant in each flight, though they are allowed to vary between flights, so as to account for variation of input amplitude between flights. The weighting matrix is manually chosen to suitably balance the errors between translational acceleration and angular acceleration.

$$W = diag\,(140, 140, 140, 0, 0, 0, 1, 1, 1, 0, 0, 0) \tag{21}$$

The steepest descent algorithm produces a set of optimized parameters Θ^* (tabulated in Table I) with the average residual error $S = (1.65 \pm 0.81) \times 10^4$ (the uncertainty indicates one standard deviation between flights).

It can be seen that C_t, C_b and C_w are considerably smaller than unity. One possible explanation is that effective area

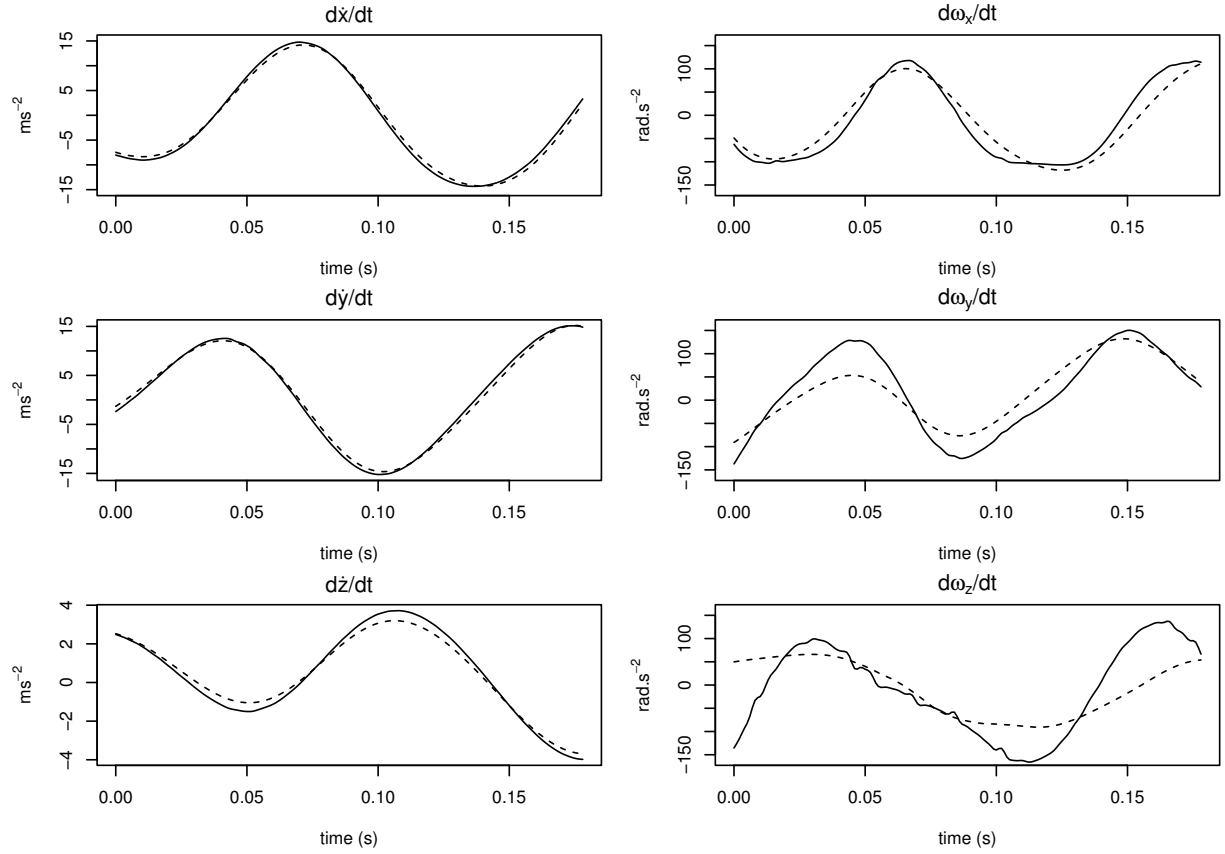

Fig. 5. Comparison between the measured (solid lines) and predicted (dashed lines) translational and angular accelerations obtained from the steepest descent algorithm. Shown in the figure is the data from one flight, which has an average residual error of 2.31×10^4.

TABLE I

PHYSICAL PARAMETERS FROM TWO OPTIMIZATION REGIMES

Symbol	Θ^*	$\Theta^\#$	Units
Constant parameters			
m	121	121	mg
l_t	20.0	20.0	mm
l_b	15.0	15.0	mm
v_w	6.09	6.09	m·s^{-1}
S_w	52.2	52.2	mm^2
Optimized parameters			
I_{xx}	2.282×10^{-8}	2.366×10^{-8}	kg·m^2
I_{yy}	2.432×10^{-8}	2.492×10^{-8}	kg·m^2
I_{zz}	2.553×10^{-9}	2.683×10^{-9}	kg·m^2
C_t	0.384	0.440	-
C_b	0.289	0.276	-
C_w	0.657	0.696	-
c_z	5.14×10^{-4}	4.80×10^{-4}	kg·m^{-1}
$c_{z\omega}$	7.63×10^{-6}	7.91×10^{-6}	kg
$c_{z\omega^2}$	6.40×10^{-9}	6.20×10^{-9}	kg·m
$c_{\omega z}$	2.20×10^{-6}	2.05×10^{-6}	kg
d_t	15.13	15.76	mm
d_b	-23.54	-23.62	mm
d_w	0.16	0.17	mm
r_{cp}	3.98	3.87	mm
F_x^t	0.198 ± 0.040	0.200 ± 0.040	mN
F_y^t	-0.174 ± 0.035	-0.177 ± 0.039	mN
F_z^t	1.318 ± 0.043	1.311 ± 0.050	mN
τ_x^t	-5.55 ± 58	-5.52 ± 76	μNm
τ_y^t	1.73 ± 56	1.71 ± 62	μNm
τ_z^t	1.21 ± 14	1.24 ± 15	μNm

of the dampers and the wing planform area are, in fact, smaller than their physical areas. In the case of dampers, it is because each plate is split into two halves by the orthogonal plate, hence the flow parallel to the plate is disrupted by the second plate. The effective wing planform area is reduced by the passive rotation of the wings, which is ignored in the proposed model. In the mean time, the downwash from flapping wings may play a part in rendering C_b to be slightly smaller than C_t.

The distance from the center of mass to the center of the top damper, bottom damper, and wings (d_t, d_b and d_w) are within a few millimeters of the calculated values from a CAD model. Similarly, the identified moment of inertia values are within 5% of those computed values. The discrepancy is likely caused by manual fabrication processes and simplifications made in the aerodynamic model.

Fig. 5 shows a comparison between measured accelerations and predicted accelerations made by the identified model. It can be seen that the proposed model is capable of predicting both translational and angular accelerations reasonably well. However, the predictions for angular accelerations reveal some degree of disagreement with the measurements. This is likely a consequence of a fast yaw rotation rate ($\omega_z \approx$ 30-60rad·s^{-1}) exhibited by the robotic insect due to its inherent yaw torque, presumably arising from manufacturing imperfections.

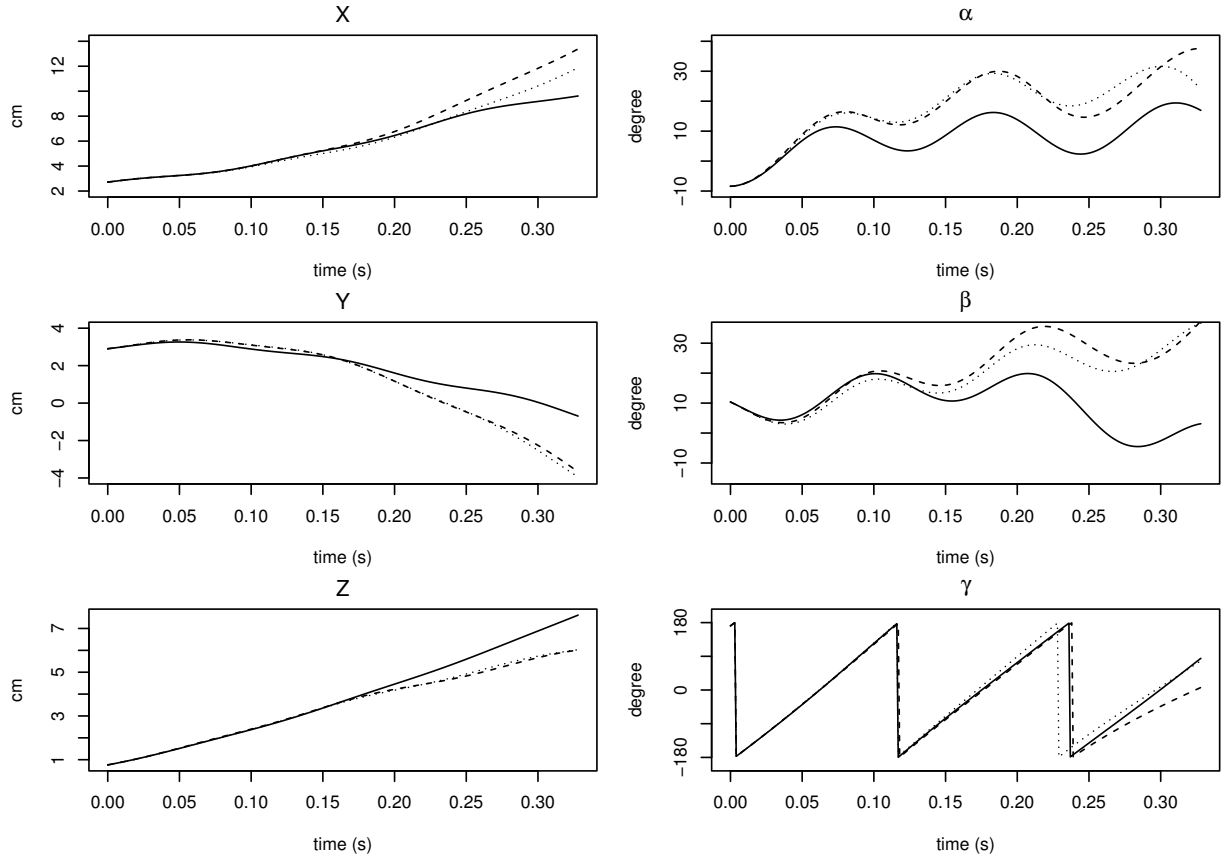

Fig. 6. Comparison between the measured trajectory of one flight (solid lines), the trajectory simulated from the initial condition using the set of parameters (Θ^*) from the optimization in section IV-C (dashed lines), and another trajectory simulated using the set of parameters ($\Theta^{\#}$) refined for predicting long-term trajectories (dotted lines). The refinement algorithm reduces the average error of this flight from 5.75 to 3.67.

D. Model refinement

The steepest descent algorithm employed in the previous section searches for a set of parameters that minimize the objective function in equation (20). The interpretation is that the algorithm finds an optimal model for predicting the accelerations of the system on a one time step basis. Nevertheless, ultimately, a model that accurately predicts long term behaviors of the system is desired. Motivated by [11], [12], here we consider another optimization problem: minimizing the error between the state vectors computed by simulating the state forward from an initial condition and the observations. Mathematically, this can be written as

$$\begin{aligned} e_i &= \mathbf{X}_{i,measurement} - \mathbf{X}_{i,simulation} \\ \Theta^{\#} &= \underset{\Theta}{\operatorname{argmin}}\ G \\ &= \underset{\Theta}{\operatorname{argmin}}\ \frac{1}{N}\sum_{i=1}^{N} e_i^T Q^2 e_i, \end{aligned} \tag{22}$$

where

$$Q = diag\,(0,0,0,1,1,1,0,0,0,140,140,140)\,. \tag{23}$$

Again, this optimization is carried out to compute one set of parameters that satisfy all 12 flights at once. However, since Jacobian matrices are unavailable, this prevents the use of the steepest descent method. Alternatively, a stochastic gradient descent is selected to minimize the average residual error G. Notice that the weighting matrix is deliberately chosen to be consistent with that of equation (20).

The optimization process is initialized with $\Theta = \Theta^*$, resulting in the average error $G = 5.75 \pm 5.77$. Large variation between flights is partially due to different flight durations. The optimization returns a set of optimized parameters $\Theta^{\#}$ (also listed in Table I) that brings down the average error to 3.76 ± 2.82 with subtle changes in values. Fig. 6 demonstrates one example of optimized predictions of the flight trajectory. At the first glance, the stochastic gradient descent seems to bring a modest improvement into the predictions, however the improvement in γ, which is not easily noticeable due to the scale, is quite dramatic. Overall, the result reveals an impressive predictive ability of the model for a prediction up to $\sim$ 50ms into the future. This is significantly larger than the current latency of the motion capture system.

V. Discussion and Future Work

This paper presents a physics-based nonlinear model describing the dynamics of insect scale flapping-wing robots with attached air dampers. Model parameters are identified using learning methods by comparing the model's prediction to recorded flight trajectories in the time domain. It is shown

that the identified model is capable of accurately capturing the dynamics of the system. This is a significant development from the two-dimensional simplified model presented in [6], [20].

Not only does the model describe the aerodynamics of the robotic bee, the approach also enables us to identify some physical parameters, such as moment of inertia or the center of mass, that are otherwise difficult to measure at this scale. Predicted values from CAD software cannot be taken for granted due to imperfect fabrication methods.

The resultant model can serve as a tool for controller design or to quickly identify a robot's properties before flight experiments to account for variation between robots. The fact that the model is modular and physics-based, it could predict the system's behavior when the dampers are modified or removed. This would allow us to predict the optimal damper size and placement to achieve robust stabilization within given mass constraints.

In the future, it is possible to implement the model in the estimator part of the control loop, using a nonlinear filter, such as the extended or unscented Kalman filter. The use of such a filter will alleviate sporadic disturbance problems in the motion tracking system when it briefly loses tracking. Additionally, the estimator could serve as a predictor to counter the latency of the control and measurement system. In [17], it was claimed that a similar system suffered from 35ms loop delay. Recent analysis suggests that the lower bound of the latency in our control loop is 10ms (approximately one wing beat), but this value could grow significantly as the controller becomes more sophisticated or the tracking system is substituted by other sensing systems, such as onboard ocelli, gyroscopes or optical flow sensors.

VI. Acknowledgments

The authors thank Zhi Ern Teoh for advice and help on fabrication of the robot, and Sawyer Fuller for technical consultation and preparation of the manuscript.

References

[1] G. De Croon, K. De Clercq, R. Ruijsink, B. Remes, and C. De Wagter, "Design, aerodynamics, and vision-based control of the Delfly," *International Journal of Micro Air Vehicles*, vol. 1, no. 2, pp. 71–97, 2009.

[2] M. Keennon, K. Klingebiel, H. Won, and A. Andriukov, "Development of the nano hummingbird: A tailless flapping wing micro air vehicle," in *50th AIAA Aerospace Sciences Meeting including the New Horizons Forum and Aerospace Exposition*, pp. 1–24, 2012.

[3] R. Wood, B. Finio, M. Karpelson, K. Ma, N. Perez-Arancibia, P. Sreetharan, H. Tanaka, and J. Whitney, "Progress on "pico" air vehicles," *The International Journal of Robotics Research*, 2012.

[4] N. Pérez-Arancibia, K. Ma, K. Galloway, J. Greenberg, and R. Wood, "First controlled vertical flight of a biologically inspired microrobot," *Bioinspiration & Biomimetics*, vol. 6, p. 036009, 2011.

[5] P. Sreetharan, J. Whitney, M. Strauss, and R. Wood, "Monolithic fabrication of millimeter-scale machines," *Journal of Micromechanics and Microengineering*, vol. 22, no. 5, p. 055027, 2012.

[6] Z. Teoh, S. Fuller, P. Chirarattananon, N. Perez-Arancibia, J. Greenberg, and R. Wood, "A hovering flapping-wing microrobot with attitude control and passive upright stability," to appear *Intelligent Robots and Systems (IROS), 2012 IEEE/RSJ International Conference on*.

[7] B. Finio and R. Wood, "Open-loop roll, pitch and yaw torques for a robotic bee," to appear *Intelligent Robots and Systems (IROS), 2012 IEEE/RSJ International Conference on*.

[8] K. Ma, S. Felton, and R. Wood, "Design, fabrication, and modeling of the split actuator microrobotic bee," to appear *Intelligent Robots and Systems (IROS), 2012 IEEE/RSJ International Conference on*.

[9] M. Tischler and R. Remple, *Aircraft and rotorcraft system identification*. American Institute of Aeronautics and Astronautics, 1801 Alexander Bell Drive, Suite 500, Reston, VA, 20191-4344, USA,, 2006.

[10] V. Klein, E. Morelli, A. I. of Aeronautics, and Astronautics, *Aircraft system identification: theory and practice*. American Institute of Aeronautics and Astronautics, 2006.

[11] W. Hoburg and R. Tedrake, "System identification of post stall aerodynamics for UAV perching," 2009.

[12] P. Abbeel, V. Ganapathi, and A. Ng, "Learning vehicular dynamics, with application to modeling helicopters," *Advances in Neural Information Processing Systems*, vol. 18, p. 1, 2006.

[13] J. Grauer, E. Ulrich, J. Hubbard, D. Pines, and J. Humbert, "Testing and system identification of an ornithopter in longitudinal flight," *Journal of Aircraft*, vol. 48, no. 2, pp. 660–667, 2011.

[14] J. Niño, F. Mitrache, P. Cosyn, and R. De Keyser, "Model identification of a micro air vehicle," *Journal of Bionic Engineering*, vol. 4, no. 4, pp. 227–236, 2007.

[15] G. Arfken, H. Weber, and F. Harris, *Mathematical Methods for Physicists: A Comprehensive Guide*. Academic press, 2012.

[16] F. van Breugel, W. Regan, and H. Lipson, "From insects to machines," *Robotics & Automation Magazine, IEEE*, vol. 15, no. 4, pp. 68–74, 2008.

[17] R. Cory and R. Tedrake, "Experiments in fixed-wing UAV perching," in *Proceedings of the AIAA Guidance, Navigation, and Control Conference*, 2008.

[18] S. Sane and M. Dickinson, "The aerodynamic effects of wing rotation and a revised quasi-steady model of flapping flight," *Journal of Experimental Biology*, vol. 205, no. 8, pp. 1087–1096, 2002.

[19] J. Whitney and R. Wood, "Aeromechanics of passive rotation in flapping flight," *Journal of Fluid Mechanics*, vol. 660, no. 1, pp. 197–220, 2010.

[20] A. Bergou, S. Xu, and Z. Wang, "Passive wing pitch reversal in insect flight," *Journal of Fluid Mechanics*, vol. 591, pp. 321–338, 2007.